MATERIALS CHEMISTRY FRONTIERS

CHINESE CHEMICAL SOCIETY

ROYAL SOCIETY OF CHEMISTRY

RESEARCH ARTICLE

View Article Online
View Journal | View Issue

Cite this: *Mater. Chem. Front.*, 2023, **7**, 5005

Porous yet densely packed metal–organic frameworks (MOFs) toward ultrastable oxygen evolution at practical current densities†

Haiming Wang,[ab] Ming Li,[a] Jingjing Duan [a] and Sheng Chen *[a]

Received 30th May 2023,
Accepted 13th August 2023

DOI: 10.1039/d3qm00614j

rsc.li/frontiers-materials

It is known that the increase of catalyst loadings usually leads to activity decay owing to the increased mass transport limitations. And most catalyst electrodes are thus restricted to small mass loadings (0.1–1 mg cm^{-2}). However, there are exceptions. Here we have reported the confined growth of nickel, iron-metal–organic framework (NiFe-MOF) electrodes characteristic of porous yet densely packed architectures. The NiFe-MOF electrode has shown elevated activities for the catalyst loadings increasing from 1 to 10 mg cm^{-2}, and achieving excellent oxygen evolution at the practical levels of catalyst loading (~10 mg cm^{-2}). Further detailed study reveals the NiFe-MOF electrode is composed of self-assembled MOF nanoribbons in 3D honeycomb architecture on a nickel foam substrate. The electrode can afford hierarchical macro–micro-porosity that facilitates fast mass transport, in addition to high catalyst loadings for securing strong durability. Consequently, NiFe-MOF electrodes are optimized to deliver the best oxygen evolution activities ever reported for MOFs, characteristic of a low overpotential of 226 mV at 10 mA cm^{-2}, and a prolonged stability up to 666 h at 100 mA cm^{-2} or 100 h at 500 mA cm^{-2}.

1. Introduction

Water electrolysis has the advantage of producing "green" hydrogen without carbon dioxide emission, which is expected to solve the problem of global warming caused by fossil fuels.[1–3] Generally, water electrolysis is comprised of two half-cell reactions, the anodic oxygen evolution reaction (OER, $4OH^- \rightarrow O_2 + 2H_2O + 4e^-$) and cathodic hydrogen evolution reaction (HER, $2H_2O + 2e^- \rightarrow H_2 + 2OH^-$).[2–4] In comparison to HER, the OER is a more energy-intensive reaction because it proceeds *via* a four-proton–electron coupled pathway, and hence requires a higher external overpotential to overcome sluggish reaction kinetics.[1,5] For OER electrocatalysts, activity, stability and cost are the three critical merits that need to be considered for practical applications. In industry, noble metal catalysts (like ruthenium oxide RuO_2[1,5,6] and iridium dioxide IrO_2[5,6]) have been used as the benchmark catalysts to facilitate OER, but their high cost and scarcity limit large-scale applications. As a consequence, a variety of cost-effective alternatives (such as transition metal oxides[7,8] and carbons[8]) have been developed. However, the OER activities and stability of these catalysts still need to be further enhanced for practical water electrolysis.

Typically, the OER process consists of three intermediate steps: (i) H_2O migrates to the surfaces of electrodes, (ii) H_2O splitting to O_2 through a proton–electron coupling step, and (iii) O_2 evolution from electrodes.[9–11] Therefore, the activity and stability of OER should be related to such factors as the number of active centres and mass/charge transport of H_2O and O_2.[5,9–12] Currently, most OER catalytic electrodes have been prepared into thin films, and their thickness has been reduced to nanometre levels to maximize the exposure of catalytic active centers and facilitate mass/charge transfer kinetics. However, such thin-film electrodes (0.1–1 mg cm^{-2}, mass loadings) are not able to meet the requirement for practical applications (greater than 1 mg cm^{-2}).[13] In bulk water electrolysis especially under high current conditions ($\geq$500 mA cm^{-2}), these thin-film electrodes are prone to performance decline due to bubble effects and loss of active centres, *etc.*[5,6] Although thicker electrodes can be fabricated by directly increasing the mass loading (greater than 1 mg cm^{-2}) using the same preparation procedure, significant problems may also occur, for example, the increased mass transport limitations in thick electrodes and active species peeling off from electrodes because of weak catalyst–substrate interactions, leading to sharp activity drop in proportion to mass loadings.[5,6,13]

In nature, honeycombs are important habitual residences for bees to rest, breed and store foods. In order to facilitate the

[a] *Key Laboratory for Soft Chemistry and Functional Materials (Ministry of Education), School of Chemical Engineering, School of Energy and Power Engineering, Nanjing University of Science and Technology, Nanjing, Jiangsu 210094, China. E-mail: sheng.chen@njust.edu.cn*

[b] *College of Mechanical and Electronic Engineering, Tarim University, Alaer, Xinjiang 843300, China*

† Electronic supplementary information (ESI) available. See DOI: https://doi.org/10.1039/d3qm00614j

frequent entry and exit of bees, honeycombs are usually constructed with highly porous structures. Simultaneously, to store as much foods as possible and accommodate more offspring, the honeycombs are also arranged with densely packed architectures.[14,15] Inspired by the honeycomb structures, we consider the construction of porous yet densely packed electrodes may be one of the ways to improve the electrocatalytic activity and stability of thick electrodes. Recently, metal–organic frameworks (MOFs) have become a new class of functional materials. MOFs have the advantages of abundant intrinsic molecular metal sites, rich porosity, large specific surface areas, and characteristics of inorganic–organic structural units, which are useful for water electrolysis.[1–3] By adjusting the packing styles of MOFs, the porous yet densely packed MOF electrodes would allow rapid mass transfer under high mass loadings, which is rarely reported thus far.

In this work, we report a confined growth procedure to assemble NiFe-MOFs with characteristics of hierarchical porosity (micropore, and macropore) and high packing density (up to 10 mg cm^{-2}). The OER performances of NiFe-MOF electrodes are optimized to deliver a low overpotential of 226 mV at 10 mA cm^{-2}, and a prolonged stability up to 666 h at 100 mA cm^{-2} or 100 h at 500 mA cm^{-2}, which would play a positive role in the industrial applications of water electrolysis.

2. Experimental

2.1 Chemicals

2-Hiophenecarboxylic acid (2-$C_5H_4O_2S$, 99%) was purchased from Tianjing Heowns Biochemical Technology Co., Ltd. Nickel acetate tetrahydrate ($Ni(Ac)_2{\cdot}4H_2O$, 99%), ferric(III) nitrate nonahydrate ($Fe(NO_3)_3{\cdot}9H_2O$, 98.5%) and sodium hydroxide (NaOH, 95%) were obtained from Shanghai Macklin Biochemical Technology Co., Ltd. Ethanol (absolute alcohol, AR) was purchased from Sinopharm Chemical Reagent Co., Ltd. IrO_2 were obtained from Afar Aesa. All chemicals were used as they were received from manufacturers. All aqueous solution was prepared with high-purity de-ionized water (DI–water, resistance 18.25 MΩ cm^{-1}). Nickel foam (NF, 2.8 cm × 2 cm × 1.6 mm, surface density 380 g m^{-2}, PPI 110, porosity >95%, purity 99.8%) was purchased from Suzhou Sinero Technology Co., Ltd. Nickel foam was washed successively with dilute HCl solution, absolute alcohol and DI–water under ultrasonication for 5 min, respectively, which was used to remove the surface oxide layer and organic residue. Then the clean nickel foam was immersed in absolute alcohol for use.

2.2 Synthesis of materials

2.2.1 Synthesis of NiFe-MOF honeycombs. 600 mg of organic ligand (2-$C_5H_4O_2S$), 540 mg of $Ni(Ac)_2{\cdot}4H_2O$ and 60 mg $Fe(NO_3)_3{\cdot}9H_2O$ were added to 30 mL of absolute ethanol under magnetically stirring for several hours. Next, the above solution was poured into a 50 mL Teflon-lined autoclave where a piece of clean nickel foam (NF, 2.8 cm × 2 cm × 1.6 mm) was immersed into autoclave titling against wall. Then, the autoclave was sealed and maintained at 150 °C for 12 h. After naturally cooling down to room temperature, the yellow NiFe-MOF honeycombs on nickel foam substrate were taken out, and the corresponding precipitates in the autoclave solution were separated by centrifugation. Both of them were washed alternately with deionized H_2O and absolute ethanol several times, and finally dried at 60 °C overnight.

2.2.2 Synthesis of other NiFe-MOF honeycombs with different Fe wt%. Other NiFe-MOF honeycombs (denoted as 5%, 15%, and 20% Fe) with were prepared similarly to NiFe-MOF but using different amounts of Fe precursors. Specifically, NiFe-MOF-5% was prepared by using 570 mg of $Ni(Ac)_2{\cdot}4H_2O$ and 30 mg $Fe(NO_3)_3{\cdot}9H_2O$; NiFe-MOF-15% was obtained by using 510 mg of $Ni(Ac)_2{\cdot}4H_2O$ and 90 mg $Fe(NO_3)_3{\cdot}9H_2O$; NiFe-MOF-20% was synthesized by using 480 mg of $Ni(Ac)_2{\cdot}4H_2O$ and 120 mg $Fe(NO_3)_3{\cdot}9H_2O$.

2.2.3 Synthesis of NiFe-MOF honeycomb catalysts with different mass loadings. NiFe-MOF honeycombs with different mass loadings (1.11,3.12,6.22,9.95,12.06 mg cm^{-2}, denoted as NiFe-MOF-1, NiFe-MOF-3, NiFe-MOF-6, NiFe-MOF, NiFe-MOF-12; Tables S5–S9, ESI†) were prepared by a similar method by using different amounts of precursors. Specifically, NiFe-MOF-1 with an average mass loading of 1.11 mg cm^{-2} was prepared by using 90 mg of $Ni(Ac)_2{\cdot}4H_2O$, 10 mg $Fe(NO_3)_3{\cdot}9H_2O$ and 100 mg 2-$C_5H_4O_2S$; NiFe-MOF-3 with an average mass loading of 3.12 mg cm^{-2} was obtained by using 180 mg of $Ni(Ac)_2{\cdot}4H_2O$, 20 mg $Fe(NO_3)_3{\cdot}9H_2O$ and 200 mg 2-$C_5H_4O_2S$; NiFe-MOF-6 with an average mass loading of 6.22 mg cm^{-2} was synthesized by using 360 mg of $Ni(Ac)_2{\cdot}4H_2O$, 40 mg $Fe(NO_3)_3{\cdot}9H_2O$ and 400 mg 2-$C_5H_4O_2S$; NiFe-MOF-12 with an average mass loading of 12.06 mg cm^{-2} was synthesized by using 720 mg of $Ni(Ac)_2{\cdot}4H_2O$, 80 mg $Fe(NO_3)_3{\cdot}9H_2O$ and 800 mg 2-$C_5H_4O_2S$.

2.2.4 Synthesis of Ni-MOF honeycombs. Ni-MOF honeycombs (denoted as Ni-MOF) were prepared similarly to NiFe-MOF but using only the nickel precursors.

2.2.5 Synthesis of bulk NiFe-MOF. Bulk NiFe-MOF (denoted as bulk) was obtained by drying the precipitates during the synthesis of NiFe-MOF honeycombs. To fabricate catalyst electrodes, bulk NiFe-MOF powders were dispersed in isoproponal/water (V_i/V_w = 3/1) mixed solvents with 1 wt% Nafion as the binder, and then being drop casted onto a nickel foam substrate with mass loading of 10 mg cm^{-2}.

2.2.6 Synthesis of IrO_2 catalyst ink. Synthesis of IrO_2 catalyst electrode was similar to bulk NiFe-MOF but using IrO_2 powder as the active component.

2.3 Physical characterizations

Scanning electron microscopy was conducted on a field emission scanning electron microscope (FESEM, JEOL 7800F). Transmission electron microscope (TEM) and high-resolution transmission electron microscope (HRTEM) were conducted on an aberration-corrected TEM (Thermo Scientific-Talos™ F200i, 200 kV acceleration Voltage). Energy-dispersive X-ray spectroscopy (EDS) and element mapping were acquired on SEM (OXFORD X-Max^N 150 10 kV). X-ray diffractions were conducted on X-ray diffractometer (XRD, Bruker-AXS D8 Advance 3 kW, 40 kV, 40 mA, λ = 1.5418 Å) with Cu Kα radiation. X-ray photoelectron spectroscopy

(XPS) was collected between 4 and 200 eV on an Axis Ultra (ThermoScientific™ K-Alpha) XPS spectrometer equipped with an Al Kα source (1486.6 eV). FTIR spectra were recorded in a Thermofisher NICOLETIS 20 FTIR spectrometer. Inductively coupled plasma mass spectroscopy (ICP-MS) measurements were carried on Agilent 7800. Atomic Force Microscopy (AFM) was conducted on Bruker Dimension ICON SPM using peak force mode. The specific surface areas of the as-prepared products were measured on a Micromeritics® TRISTAR II 3020 instrument, and the pore size distributions were derived from the desorption branches of the isotherm with the Barrett–Joyner–Halenda (BJH) model.

2.4 Electrochemical characterizations

Electrochemical tests were performed on a CHI 760E electrochemical workstation. Specifically, OER was tested in a three-electrode system in a single electrolytic cell with 1 M KOH aqueous solution (with 85% iR-compensation), which used MOF honeycombs, graphite rod and Hg/HgO (1 M KOH) as working, counter and reference electrodes, respectively.

The OER overpotential *vs.* $E_{Hg/HgO}$ measured in this study can be converted to corresponding overpotentials using the following equation:

$$\eta = E_{Hg/HgO} + 0.059 \times pH + 0.098 - 1.23\ V$$

Linear sweep voltammogram (LSV) plots were recorded at a scan rate of 5 mV s^{-1} from 1.7 to 0.9 V (*vs.* RHE, reverse scans). All LSV plots were recorded with 85% iR-compensation. The Tafel slope was calculated according to Tafel equation as follows:

$$\eta = b \log j + a$$

where η is overpotential (V), j is current density (mA cm^{-2}), and b is Tafel slope (mV dec^{-1}).

The long-term durability was tested by chronopotentiometry at 100 mA or 500 mA for OER up to 666 h. The corresponding LSVs before and after electrochemical testing were collected with 85% iR-compensation for comparison purpose. In addition, electric double layer capacitances (C_{dl}, mF cm^{-2}) of working electrodes were obtained from double-layer charge–discharge diagram using cyclic voltammetry (CV) in a small potential range of 1.219–1.319 V (*vs.* RHE). Both a plot of the $\Delta J = (J_a - J_c)/2$(mA) at 1.269 V (*vs.* RHE) against scan rate are nearly linear and the double layer capacitance were obtained by its slopes. Based on the reported method, we have used a benchmark capacitance of C_s = 0.04 mF cm^{-2} (typical reported value) to calculate electrochemically active surface area (ECSA, denoted as A_{ECSA}) of various electrodes ($A_{ECSA} = C_{dl}/C_s$ (per cm^{-2})).[16] The use of geometric area (GA, denoted as A_{GA}) for current normalization (denoted as J_{GA}) could be traced back to the period when smooth planar electrodes were widely used in the electrochemical community, and it could be calculated based on the dimension of the surface contacting the electrolyte: $A_{GA} = 2hl + wl + 2wh$.[17] In most cases, the thickness of the planar electrode is much smaller than its length and height, thus $A_{GA} \approx 2hl$, A_{GA} is 1 cm^2 in this work (A_{GA} = 2 × 0.5 cm × 1 cm = 1 cm^2). Electrochemical impedance spectroscopy (EIS) was measured at 1.295 V (*vs.* Hg/HgO) from 100 KHz to 0.01 Hz. Faraday efficiency (FE) was measured in a H-type electrolytic cell with MOF honeycombs, graphite rod and Hg/HgO (1 M KOH) as anode, cathode and reference electrodes, respectively. FE was calculated based on the equation: $FE = V_{exp.}/V_{the.} = V_{exp.}/(V_m\ Q/(n\ F)) = V_{exp.}/(V_m\ i\ t/(n\ F))$, where $V_{exp.}$ is the experimental volume of O_2, $V_{the.}$ is the theoretical volume of O_2, V_m is the molar volume of gas (25 °C, 24.5 L mol^{-1}), Q is the amount of electric charge, n is the number of electrons transferred; F is Faraday constant (96,485 C mol^{-1}); i is the test current, t is the collection time of O_2.[18]

3. Results and discussion

3.1 Synthesis and growth of NiFe-MOF

The preparation procedure is shown in Scheme 1. NiFe-MOF honeycombs were prepared by a one-step confined growth approach starting by coordinating highly concentrated precursor solution composed of metal salts (Fe, Ni) and organic ligands

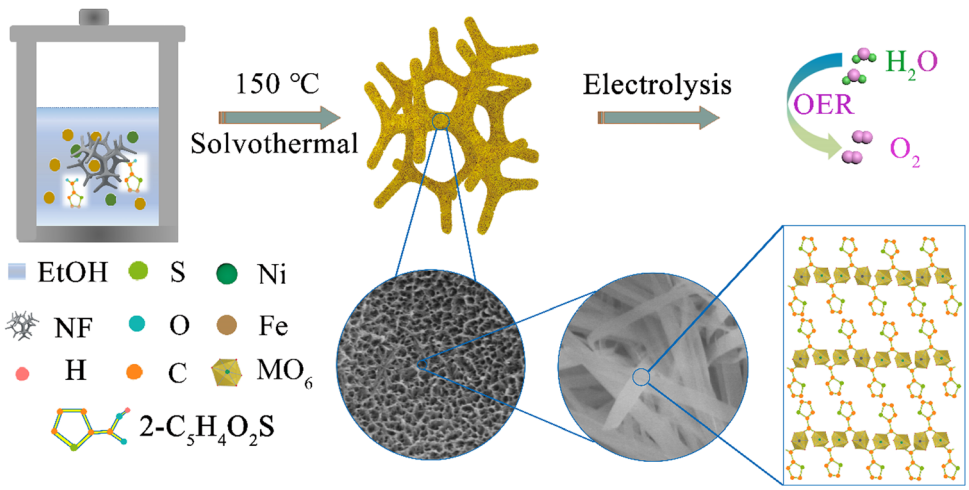

Scheme 1 Confined growth of NiFe-metal–organic framework (MOF) electrode.

(2-$C_5H_4O_2S$). According to the characterizations of XRD (Fig. 1(a) and Fig. S1, ESI†), SEM (Fig. 1(c)–(e) and Fig. S2, ESI†), TEM (Fig. 1(f) and (g)), AFM (Fig. S3, ESI†), FTIR (Fig. 1(b) and Fig. S4, ESI†) and XPS (Fig. S5, ESI†), the as-prepared NiFe-MOF honeycombs are composed of nanoribbons, which are further constructed by alternating organic units (2-thiophenecarboxylic acid group) and inorganic units (NiO_6 or FeO_6). The carboxyl group on each ligand bridges two transition metal ions, and each ion coordinates with two opposite carboxyl groups and four equatorial ethanol molecules.

We then used SEM and elemental mappings to study the confined growth process. The growth process of NiFe-MOF was explored by elongating reaction durations from 0.5 to 16 h (Fig. S6, ESI†). Firstly, irregular nano-particles without apparent elemental segregation are observed in the NiFe-MOF intermediate obtained at 0.5 h, indicating that metal ions and ligands begin to nucleate within this period (Fig. S6a and b, ESI†). When the reaction time was further extended, the mixtures of irregular nano-particles and nanoribbons (NRBs) are observed in the reacting intermediates collected at 2–8 h, indicating the occurrence of a crystal growth process (Fig. S6c–h and S7a–d). After 12 h of reaction, well-defined NiFe-MOF NRBs have formed that fill into nickel foam, and the morphology and size alternation of NRBs are negligible within this period (Fig. S6i–l and S7e, f, ESI†).

3.2 Structure and morphology characterizations of NiFe-MOF

According to the volcano plots, Ni-based materials have moderate binding energies, next only to the noble-based catalysts, thereby indicating a small theoretical overpotential for the OER.[3,19] Among the numerous reported 3d transition metal-based electrocatalysts, Ni/Fe-based materials are known as highly active sites for OER. Compared with noble metals (RuO_2/IrO_2), Ni/Fe transition metal-based elements are earth-abundant, cheap, and easy to large-scale application.[3,4,19–22] Because Ni and Fe are known as highly active sites for OER,[3,4,18,21] the as-formed NiFe-MOFs were further characterized. Firstly, according to ICP analyses, the content of nickel and iron in the product can be accurately determined (Table S1, ESI†). Next, the crystal structure of NiFe-MOF honeycombs (Fig. S1, ESI†) was characterized by XRD, which shows a well-defined MOF crystal structure as well as strong substrate (NF) peaks at around 44.73°, 52.09°, and 76.64°. The strongest diffraction peak at 2θ = 6.48° is ascribed to (020) plane of NiFe-MOF honeycombs (Fig. 1(a) and Fig. S1, ESI†).[23] Other comparison MOFs also show similar XRD patterns (Fig. S1, ESI†). This result is consistent with FTIR spectra that confirm the strong coordination interactions between metal ions and organic ligands in MOFs (Fig. 1(b)). According to the literature[4,23–26] and FTIR atlas database (Aldrich catalog no: T3260-3, CAS number: 527-72-0), the peak at around 800 cm^{-1} was the fingerprint region, which can be assigned to thiophene ring. The strong FTIR bands centered at 1584, 1521, 1372,and 775 cm^{-1} are assigned to stretching modes of carboxylate groups (COO^-) coordinated to Ni^{2+} or Fe^{3+}.[4,23–25] The FTIR bands at 1420 and 1039 cm^{-1} are attributed to in-plane ring vibration of organic ligand (2-thiophene dicarboxylic acid).[4,26] The broad band at 3610 cm^{-1} is assigned to ν(O–H) stretching vibration of water molecules.[23] Notably, the characteristic FTIR band of the acidic

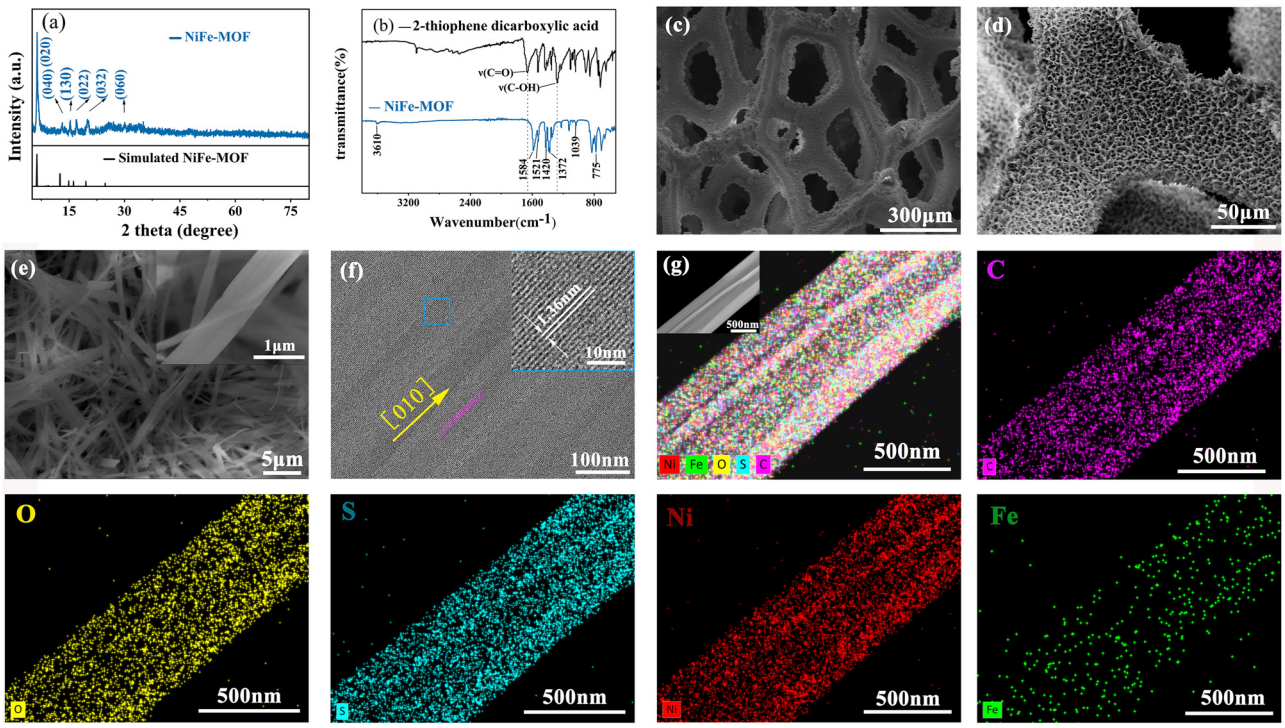

Fig. 1 Morphological and structural characterizations of NiFe-MOF. (a) experimental and simulated XRD patterns. (b) FT-IR spectra. (c)–(e) SEM images, inset of (e) is a nanoribbon; (f) and the inset of (f) HRTEM image of the NiFe-MOF with lattice fringes; (g) TEM element mappings of C, O, S, Ni, and Fe.

carbonyl group (C═O) at 1662 cm^{-1} and tensile vibration of the non-ionized carboxyl group (C–OH) at 1278 cm^{-1} have disappeared, indicating that the organic ligand (2-thiophene dicarboxylic acid) is completely deprotonated by coordinating with metal ions.[4,23,26] Other MOFs have shown similar FTIR vibration characteristics to NiFe-MOF (Fig. S4, ESI†).

In addition, X-ray photoelectron spectroscopy (XPS) was further employed to investigate the surface elemental compositions and electronic states of the samples. As shown in Fig. S5a (ESI†), the XPS survey spectra on NiFe-MOF honeycombs surface confirm the presence of C, O, S, Ni, and Fe elements, which is consistent with the results of EDS spectrum (Fig. 2(g)). High-resolution XPS spectra of C 1s, O 1s, S 2p, Fe 2p, and Ni 2p were presented in Fig. S5b–f (ESI†), respectively. Three surface components can be obtained by using deconvolution of the high-resolution spectrum of C 1s (Fig. S5b, ESI†), corresponding to the C–S of 2-hiophenecarboxylic acid at a binding energy of 284.7 eV,[27] the carboxylate (C═C) groups of 2-hiophene-carboxylic acid at a binding energy of 284.9 eV,[27] and the carboxylate (O–C═O) groups of 2-hiophenecarboxylic acid at a binding energy of 288.3 eV.[28] The high-resolution XPS spectrum of O 1s (Fig. S5c, ESI†) displays three binding energies at 530.8, 531.4,and 532.1 eV attributable to oxygen atoms on the Ni (Fe)–O bonds, characteristic peak of O═C–O, and absorbed water, respectively.[23,28] Next, the XPS of S $2p_{3/2}$ at 164.1 eV and S $2p_{1/2}$ at 165.3 eV indicate the C–S–C chemical bond in the organic ligand (Fig. S5d, ESI†).[4,23] As shown in Fig. S5e (ESI†), the binding energy values of Ni 2p show four major peaks, corresponding to Ni^{2+} (855.9/873.5 eV), and their corresponding satellite peaks (identified as "Sat") indicate the oxidation state of the Ni species as +2 (Ni^{2+}).[23] Fig. S5f (ESI†) shows the high-resolution spectrum of Fe 2p, in which the peaks in Fe 2p spectrum at 709.3, 722.9, and 714.2 eV correspond to Fe^{2+}, and Fe^{3+} respectively.[28,29] Indicating some Fe^{3+} ions are reduced to Fe^{2+} species ($Fe^{3+} + e^- \rightarrow Fe^{2+}$), while Ni atoms are oxidized to Ni^{2+} species (Ni-$2e^- \rightarrow Ni^{2+}$) (Fig. S5, ESI†).[30] Therefore, the Ni element in NiFe-MOF may come from the combined action of Ni salt and NF substrate. Importantly, the obtained NiFe-MOF feature honeycombs with hierarchical porosity composed of macropores around 300 μm originating from NF substrates (Fig. 1(c)) and open pores around hundreds of nanometers to tens of micrometers formed by adjacent NRBs (Fig. 1(d) and (e)). According to SEM and AFM, the as-prepared NiFe MOF honeycombs consist of quasi-one-dimensional (quasi-1D) ribbons with average dimensions of 15 nm in thickness (peeled from nickel foam substrate by ultrasonication for 3 min), 700 nm in width and tens of micrometers in length (Fig. 1(c)–(g) and Fig. S3, ESI†). The HRTEM displays good crystallinity of NiFe-MOF NRBs with a well-defined lattice viewed along the [010] axis (Fig. 1(f)), and a lattice spacing of 1.36 nm of (020) plane (inset of Fig. 1(f)). This result is closely matched with XRD results (Fig. 1(a)). Furthermore, TEM and SEM element mappings exhibit a homogeneously distribution of C, O, S, Ni, and Fe elements throughout NRBs (Fig. 2(g) and Fig. S2, ESI†). Other NiFe MOFs with different percentages of Fe also show similar structural features (Fig. S8–S11, ESI†).

We have further prepared a series of porous yet dense NiFe-MOFs by systematically tailoring packing densities of the NiFe-MOFs (Fig. 3(a)–(e) and Fig. S2, S12–S15, ESI†). Compared to NiFe-MOFs with different mass loadings, it can be observed that the stacking density of nanoribbons continues to increase from the loading increase from 1 to 10 mg cm^{-3}. When the packing density is ≥10 mg cm^{-3}, there is little change in the relative distributions of nanoribbons.

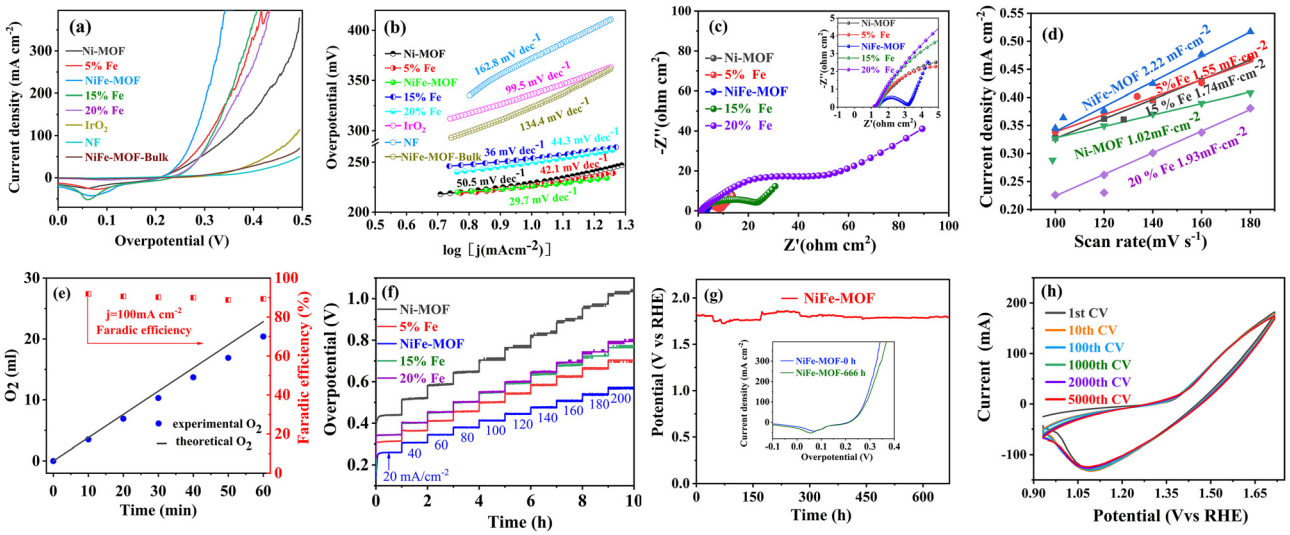

Fig. 2 The evaluation of alkaline OER electrocatalytic performances of NiFe-MOF. (a) OER LSV curves of Ni-MOF, NiFe-MOF-5%Fe, NiFe-MOF, NiFe-MOF-15%Fe, NiFe-MOF-20%Fe, NF, commercial IrO_2, and NiFe-MOF-bulk. (b) Tafel plots of different samples, (c) Nyquist plots and (d) C_{dl} values of different samples, (e) experimental and theoretical volumes of O_2 and Faraday efficiency, (f) multi-step E–t curve with the current density increased from 20 to 100 mA cm^{-2}, (g) chronopotentiometry curve of NiFe-MOF at 100 mA cm^{-2}, the inset shows LSV plots obtained before and after 666 h chronoamperometric test. (h) Cyclic voltammetry of NiFe-MOF before and after 5000 cycles.

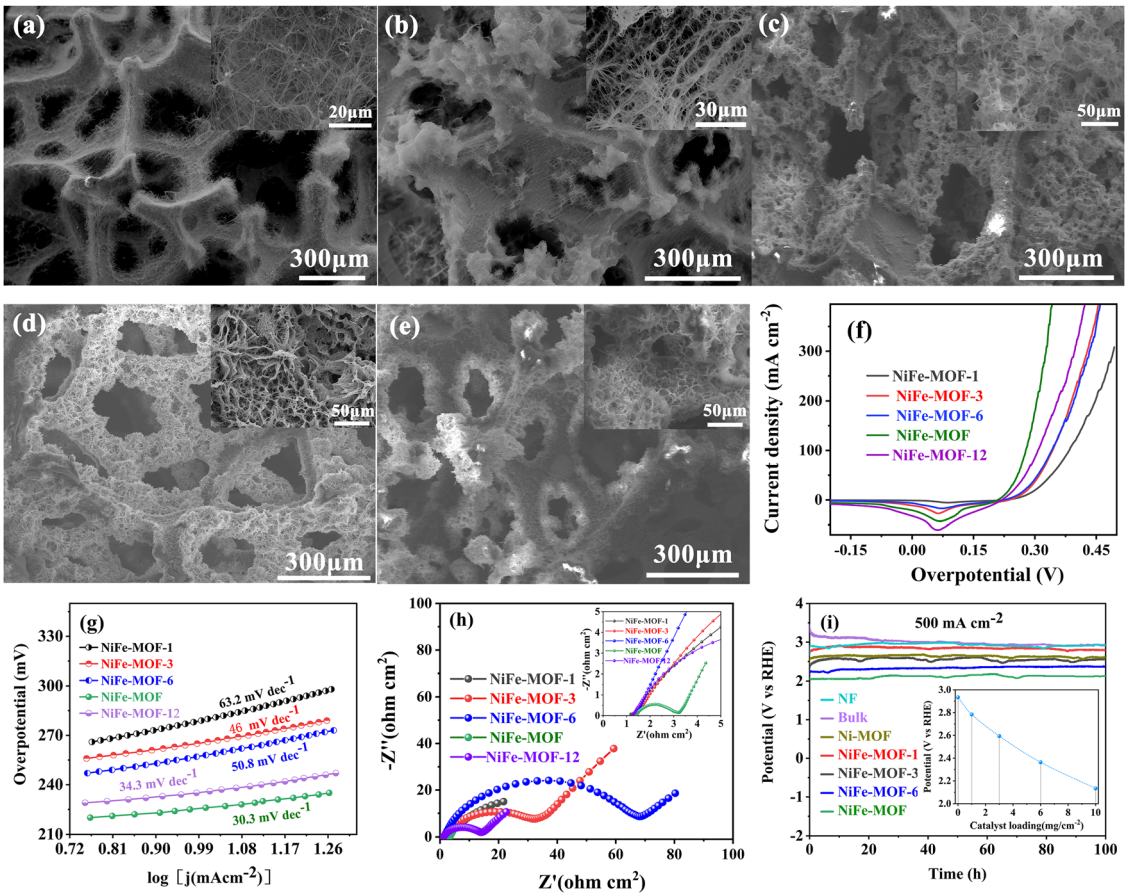

Fig. 3 Morphology characterizations and Electrocatalytic performance of alkaline OER electrocatalytic performance of NiFe-MOF with different average mass loadings. (a) SEM of NiFe-MOF-1 (b) SEM of NiFe-MOF-3 (c) SEM of NiFe-MOF-6 (d) SEM of NiFe-MOF (e) SEM of NiFe-MOF-12, (f) OER LSV curves of NiFe-MOF-1, NiFe-MOF-3, NiFe-MOF-6, NiFe-MOF, and NiFe-MOF-12. (g) Tafel plots of NiFe-MOF with different mass loadings, (h) Nyquist plots, and (i) chronopotentiometry curves of NiFe-MOFs and contrast samples at 500 mA cm^{-2}, the inset of (i) shows the potentials at 500 mA cm^{-2} as a function of catalyst loading.

3.3 Electrochemical tests for OER

All electrochemical tests for NiFe-MOF honeycombs were conducted under ambient conditions.[17,18] For comparison, several controlled experiments have been carried out under the same conditions, including NiFe-MOF with different Fe wt% (Ni-MOF, 5% Fe, NiFe-MOF, 15% Fe, 20% Fe), NiFe-MOF with different mass loadings (1, 3, 6, 10, 12 mg cm^{-2}, Tables S5–S9, ESI†), bulk NiFe-MOF counterpart, nickel foam, and commercial IrO_2. To eliminate the possible contributions of oxidation current densities of Ni^{2+}/Ni^{3+}, all linear sweep voltammetry curves (LSVs) were recorded by sweeping from both low-to-high (positive sweep) and high-to-low potentials (reverse sweep) at the scan rate of 5 mV s^{-1}, which can determine the overpotentials at small current densities accurately.[31]

As shown in Fig. 2(a) and Table S2 (ESI†), the NiFe-MOF displays catalytic activity superior to that of other comparison samples (Ni-MOF, NiFe-MOF-5%, NiFe-MOF-15%, NiFe-MOF-20%, bulk NiFe-MOF, nickel foam (NF), and IrO_2), only requiring an overpotential of 226 mV to attain the current density of 10 mA cm^{-2}. As well as these LSV curves recorded by sweeping from low to high potentials (positive sweep) (Fig. S16a, ESI†) also show similar results. The excellent OER activities of NiFe-MOF are also verified by Tafel plots (Fig. 2(b)). The NiFe-MOF demonstrates a much smaller Tafel slope of 29.7 mV dec^{-1}, as comparison to the Ni-MOF (50.5 mV dec^{-1}), NiFe-MOF-5% (42.1 mV dec^{-1}), NiFe-MOF-15% (36 mV dec^{-1}), NiFe-MOF-20% (44.3 mV dec^{-1}), bulk NiFe-MOF (134.4 mV dec^{-1}), nickel foam (162.8 mV dec^{-1}) and IrO_2 (99.5 mV dec^{-1}), indicating a high transfer coefficient and rapid electrocatalytic kinetics. To understand the origin of the high OER activities, the EIS and ECSA (C_{dl}, the ECSA is proportional to its C_{dl}) of the above electrodes have been investigated. As shown in Fig. 2(c), based on the equivalent circuit in EIS analyses (Fig. 2(c) and Table S3, ESI†),[13,32] the charge-transfer resistance (R_{ct}) of NiFe-MOF is calculated to be 1.6 Ω, which is much smaller than that of Ni-MOF (7.5 Ω), NiFe-MOF-5% (6.9 Ω), NiFe-MOF-15% (18.7 Ω), NiFe-MOF-20% (47 Ω). Further, as displayed in Fig. 2(d) and Fig. S22 (ESI†), the NiFe-MOF exhibits a C_{dl} value of 2.22 mF cm^{-2}, which is noticeably larger than those of Ni-MOF (1.02 mF cm^{-2}), NiFe-MOF-5% (1.55 mF cm^{-2}), NiFe-MOF-15% (1.74 mF cm^{-2}), NiFe-MOF-20% (1.93 mF cm^{-2}), NiFe-MOF-Bulk (0.93 mF cm^{-2}). Finally,- we have normalized the current

densities according to ECSA to reveal the intrinsic surface-area catalytic activity of these catalysts, and the NiFe-MOF still exhibits the highest OER catalytic activity (Fig. S16b, ESI†) at higher overpotential (>0.2 V). With the doping of Fe, the crystallinity of Ni-MOF gradually deteriorated (Fig. S1, ESI†), and the electrical conductivity declined.[33] Consequently, the doping of Fe cannot activate Ni-MOF at low overpotentials.[34] And Ni-MOF has a lower onset potential than other NiFe-MOF catalysts at low overpotential (0–0.2 V). While at higher overpotentials (>0.2 V), more Fe(oxy)hydroxide has formed, leading to a larger fraction of the electrolyte-permeable catalyst film participating in catalysis.[34] Both Fe^{4+} and Ni^{4+} formed to establish a synergetic effect in which the high spin d^4 Fe^{4+} stabilizes the oxyl-radical formed with Ni^{4+} through super-exchange interaction while the low spin d^6 Ni^{4+} induces the formation of O–O coupling.[35–39] As a consequence, NiFe-MOF exhibits a better activity characteristic of low overpotentials than Ni MOF at a high potential (>0.2 V). As a comparison to other counterparts, the NiFe-MOF with 20% Fe has the lowest crystallinity (Fig. S1, ESI†) and electrical conductivity,[33] owing to the formation of an insulating FeOOH phase during the electrocatalysis process.[40,41] As a consequence, these features have suppressed the oxidation peak at the overpotential of 0.2 V corresponding to the oxidation of Ni^{2+} to Ni^{3+}/Ni^{4+}.[40,41]

The Faradaic efficiency (FE) for OER was identified by directly measuring the amount of generated O_2 bubbles through a water drainage method (Fig. S17, ESI†). As shown in Fig. 2(e), the experimental O_2 volume–time curve exhibits a perfect linear relationship that matches well with the theoretical values, indicating a nearly 90% FE during the OER on NiFe-MOF. Therefore, the as-prepared NiFe-MOF is one of the most active electrocatalysts reported (Table S10, ESI†).

Importantly, we then investigated the OER performances of NiFe-MOF with different mass loadings (NiFe-MOF-1, NiFe-MOF-3, NiFe-MOF-6, NiFe-MOF, NiFe-MOF-12). As shown in Fig. 3(f)–(i), Fig. S18–S21 and Tables S2–S9 (ESI†), the NiFe-MOF sample (catalyst loading: 10 mg cm^{-2}) exhibits the best OER performance among all the samples, characteristic of the lowest overpotential (226 mV@10 mA cm^{-2}) and the smallest Tafel slope (30.3 mV dec^{-1}). We attribute the excellent performances to high transfer coefficient and rapid electrocatalytic kinetics on the NiFe-MOF electrode, as revealed by the larger C_{dl} value (2.22 mF cm^{-2}, Fig. S18a, ESI†), and the smallest R_{ct} (1.61 Ω, Fig. 3(h), Fig. S18b and Table S4, ESI†) of NiFe-MOF as comparison to other samples. These findings unambiguously highlight the superiority of the NiFe-MOF honeycombs architecture for the electrocatalytic OER performances.

Other than activities, stability is another important criterion for evaluating OER for practical applications. Accordingly, the cyclic voltammetry (CV) and chrono-potentiometry measurements were performed to investigate dynamic response and the long-term stability of NiFe-MOF and other MOFs (Ni-MOF, NiFe-MOF-5%, NiFe-MOF-15%, NiFe-MOF-20%). Fig. 2(f) shows the multi-step *i–t* curves with the current density increasing from 20 mA cm^{-2} to 200 mA cm^{-2}. As observed, the applied potentials maintain relatively stable without appreciable variations at different current densities. And NiFe-MOF shows a lower overpotential in comparison with that of the other MOFs, implying its best electrocatalytic activity. Next, the current density is fixed at 100 mA cm^{-2}, and seldom loss of the catalytic activity (<3%) for 666 h has been observed despite vigorous gas bubble evolution (Fig. 2(g)). The corresponding LSV curve of NiFe-MOF without iR compensation after the 666 h durability test shows that approximately 98% of the activity is retained, suggesting its superior durability for OER (Fig. 2(g) inset). This result is further verified by cyclic voltammetry without iR compensation of 5000 cycles (Fig. 2(h)), SEM, XRD, and FTIR (Fig. S20 and S21, ESI†).

Further, when the current density increases to industrial level (≥500 mA cm^{-2}), chronopotentiometry measurement of the long-term stability is even more important of NiFe-MOF. For bulk NiFe-MOF comparison electrode (*i.e.*, loosely packed counterpart), it shows a high initial potential at 500 mA cm^{-2}, and runs steadily after ~20 h at a potential comparable to nickel foam substrate. This means that the bulk NiFe-MOF active species have almost peeled off the surface of nickel foam in a short duration. In great contrast, other densely packed MOFs like NiFe-MOF, Ni-MOF and NiFe-MOFs with different mass loadings (NiFe-MOF-1, NiFe-MOF-3, NiFe-MOF-6) all show excellent stability. Among them, the applied external potential of NiFe-MOF is still the lowest as comparison to others (Fig. 3(i)). We note that the OER stability of the NiFe-MOF outperforms all of those previously reported MOFs (Tables S10 and S11, ESI†).

3.4 Discussion

We consider a number of unique characteristics of NiFe-MOF that contribute to excellent electrocatalytic properties. Firstly, the self-supporting catalysts often feature high electrical conductivity, and accelerated charge transfer rate.[3,21,42] This is confirmed by the large internal resistance of bulk NiFe-MOF (prepared by the Nafion-assisted drop-casting method, 30.87 Ω) than NiFe-MOF (1.6 Ω, prepared by the self-growth method on NF, Fig. 2(c), Fig. S22b and Table S3, ESI†). Secondly, there are strong interaction forces between the substrate and the active material, leading to a durable growth and uniform dispersion.[42] Nanoribbons (NRBs), as a class of quasi-1D nanostructures, have attracted both fundamental and technological interests over the past decades due to their high surface-to-volume ratio, highly active surface, and high concentration of selectively exposed crystal face.[43] For example, the NiMn-MOF aerogel self-assembled from NRBs to serve as a new generation of flexible electrocatalysts for HER from seawater splitting, which requires a low overpotential of 243 mV to achieve a current density of 10 mA cm^{-2}. What's more, the electrocatalyst remains stable catalytic performance even after being folded in half several times. The excellent performance may be attributed to the unique aerogel structure consisting of nanoribbons.[23] The as-obtained MOFs showed a quasi-1D ribbon-like morphology with thickness of 15 nm and large aspect ratio (700 nm in width and tens of micrometers in length, Fig. 2(c)–(e) and Fig. S3, ESI†). Therefore, it can expose large amounts of metal sites to act as active centres.[21]

Next, we also have found that by precisely regulating the feeding of iron of NiFe-MOF, it can dramatically enhance the charge transfer kinetics and enlarge the exposure of active sites, and remarkably decrease the resistance to charge transfer and thus promote the OER activity. The LSV curves of NiFe MOF with different Fe contents show that the OER activity of the catalyst has a volcano trend with the increase of the Fe contents. That is, the doping of Fe could increase OER activities by shifting the overpotentials of $Ni(OH)_2$ to lower regions, and the activity of the hybrid catalyst reaches best in the Fe feeding percentages of 10%. More doping of Fe could result in the formation of insulating FeOOH phase on the electrode surface, and when the Fe feeding content is higher than 25%, a significant decrease in the activity of the catalyst can be observed. According to the literature,[40,41,44] the OER rate of FeOOH electrode is slow when Fe in FeOOH was oxidized to Fe^{4+}, and the OER rate of $Ni(OH)_2$ electrode is slower when Ni in $Ni(OH)_2$ electrode was oxidized to Ni^{4+}. Therefore, when $Ni(OH)_2$ electrode was doped with appropriate amount of Fe, the OER rate of NiFeOOH electrode is the highest, which confirms the important role of iron and realized the synergistic enhancement catalytic effect of nickel–iron.[45,46] Although both NiFe-MOF and Ni-MOF have similar morphology, the smallest overpotential (226 mV@ 10 mA cm^{-2}, 278 mV@100 mA cm^{-2} for Ni-MOF *vs.* 229 mV@ 10 mA cm^{-2}, 350 mV@100 mA cm^{-2} for Ni-MOF *vs.* 372 mV@ 10 mA cm^{-2}, 494 mV@50 mA cm^{-2} for NF, Fig. 2 and Table S2, ESI†), the smallest Tafel slope (29.7 mV dec^{-1} for NiFe-MOF, 50.5 mV dec^{-1} for Ni-MOF, 162.8 mV dec^{-1} for NF), the largest C_{dl} (2.22 mF cm^{-2} for NiFe-MOF NRBs *vs.* 1.02 mF cm^{-2} for Ni-MOF and 0.31 mF cm^{-2} for nickel foam; Fig. 2 and Fig. S23, ESI†), and the smallest R_{ct} (1.6 Ω for NiFe-MOF *vs.* 7.5 Ω for Ni-MOF; Fig. 2(c) and Table S3, ESI†) values of the NiFe-MOF show the remarkable catalytic effect of iron.[3,47–49] As comparison to NiFe-MOF, nickel foam shows negligible catalytic effect for OER in terms of overpotentials (372 mV@10 mA cm^{-2}), Tafel slope (162.8 mV dec^{-1}), and C_{dl} (0.31 mF cm^{-2}).

More importantly, intimate interaction between the catalyst and 3D-support is favorable to the improvement of mass transfer, a better contact between electrolyte and catalytic interface, and effectively facilitates ion and electron transfer.[3,21,42] NiFe-MOF has a 3D honeycomb architecture, which can afford multi-dimensional hierarchical porosity to improve mass transport at electrode–electrolyte interfaces (Fig. 1(c)–(e) and Fig. S24, ESI†). Its extra-large macropores (about 300 μm) of the NF substrate can ensure the full flow of electrolytes and promote rapid transfer of as-produced O_2. And it has open pores around hundreds of nanometers to tens of micrometers formed by adjacent NRBs of MOF, which provide enormous, highly accessible catalytic active sites and short ion diffusion pathways for boosted reaction kinetics. In addition, the intrinsic fractional-scale microporosity of NiFe-MOF can also provide highly accessible molecular active sites for electrocatalytic reactions.[21]

Last but not least, the high mass loading of catalysts also has a positive effect on mechanical stability. In common electrode, high mass loadings may induce a weak contact between catalyst with electrode and the detachment of catalyst during operation.[13,50] In this work, we show a confined growth strategy for manipulating NiFe-MOF electrodes. When the mass loading is 1–10 mg cm^{-2} (industrial grade), all NiFe- based MOF catalysts can work stably at industrial current density (Fig. 3(i)). Moreover, there is a negative correlation between overpotential and mass loading (inset of Fig. 3(i)). Although it does not reflect the intrinsic activity of catalysts, it has important guiding significance in industrial application of energy saving.[50] This means that based on industrial mass loading (mg cm^{-2}), a win–win situation of low overpotential and high stability can be achieved by tailoring the NiFe-MOF honeycombs' loading scrupulously (Fig. 1(c)–(e) and 3(a)–(i)). Moreover, attributed to the honeycomb architecture with outstanding mechanical properties, such as high specific stiffness/strength, fracture toughness, and impact resistance,[14,15] porous yet densely packed NiFe-MOF honeycombs make an indelible contribution to enhancing the mechanical stability of NiFe-MOF catalysts.

4. Conclusions

In conclusion, we propose a method that is simple, efficient, and versatile, which could be used for the preparation of a series of porous yet densely packed 3D MOF electrodes. Particularly, NiFe-MOF with different Fe wt% (0%, 5%, 10%, 15%, 20%), and different mass loadings (1, 3, 6, 10, 12 mg cm^{-2}) have been prepared. The as-prepared electrodes have combined many remarkable features and exhibited significantly enhanced catalytic performances with high catalytic activity, favorable kinetics, and strong durability toward OER. This work has a positive significance in promoting MOF-based catalysts for practical applications.

Author contributions

Haiming Wang: methodology, investigation, writing original draft. Ming Li: review & editing. Jingjing Duan: writing – review & editing. Sheng Chen: conceptulization, writing – review & editing, supervision.

Conflicts of interest

The authors declare that they have no known competing financial interests or personal relationships that could have appeared to influence the work reported in this paper.

Acknowledgements

The authors would like to acknowledge the financial support from the National Natural Science Foundation (grant no. 92163124, 51888103, and 52006105), the Jiangsu Natural Science Foundation (grant no. BK20190460), and the Fundamental Research Funds for the Central Universities (grant no. 30920041113 and 30921013103). The authors thank Wenxiang Wang, Qian Zhang, and Pengxuan Zheng from Shiyanjia Lab (www.Shiyanjia.com) for the XRD, ICP and SEM measurements.

References

1 M. Chatenet, B. G. Pollet, D. R. Dekel, F. Dionigi, J. Deseure, P. Millet, R. D. Braatz, M. Z. Bazant, M. Eikerling, I. Staffell, P. Balcombe, Y. Shao-Horn and H. Schafer, Water electrolysis: From textbook knowledge to the latest scientific strategies and industrial developments, *Chem. Soc. Rev.*, 2022, **51**, 4583–4762.

2 X. Fu, R. Shi, S. Jiao, M. Li and Q. Li, Structural design for electrocatalytic water splitting to realize industrial-scale deployment: Strategies, advances, and perspectives, *J. Energy Chem.*, 2022, **70**, 129–153.

3 J. Zhao, J. J. Zhang, Z. Y. Li and X. H. Bu, Recent progress on NiFe-based electrocatalysts for the oxygen evolution reaction, *Small*, 2020, **16**, 2003916.

4 Y. Sun, S. Ding, S. Xu, J. Duan and S. Chen, Metallic two-dimensional metal-organic framework arrays for ultrafast water splitting, *J. Power Sources*, 2021, **494**, 229733.

5 Q. Wang, Y. Cheng, H. B. Tao, Y. Liu, X. Ma, D. S. Li, H. B. Yang and B. Liu, Long-term stability challenges and opportunities in acidic oxygen evolution electrocatalysis, *Angew. Chem., Int. Ed.*, 2023, **62**, e202216645.

6 F.-Y. Chen, Z.-Y. Wu, Z. Adler and H. Wang, Stability challenges of electrocatalytic oxygen evolution reaction: From mechanistic understanding to reactor design, *Joule*, 2021, **5**, 1704–1731.

7 Y. Luo, Z. Zhang, M. Chhowalla and B. Liu, Recent advances in design of electrocatalysts for high-current-density water splitting, *Adv. Mater.*, 2022, **34**, 2108133.

8 M. Tahir, L. Pan, F. Idrees, X. Zhang, L. Wang, J.-J. Zou and Z. L. Wang, Electrocatalytic oxygen evolution reaction for energy conversion and storage: A comprehensive review, *Nano Energy*, 2017, **37**, 136–157.

9 J. Song, C. Wei, Z. F. Huang, C. Liu, L. Zeng, X. Wang and Z. J. Xu, A review on fundamentals for designing oxygen evolution electrocatalysts, *Chem. Soc. Rev.*, 2020, **49**, 2196–2214.

10 Y. Zeng, M. Zhao, Z. Huang, W. Zhu, J. Zheng, Q. Jiang, Z. Wang and H. Liang, Surface reconstruction of water splitting electrocatalysts, *Adv. Energy Mater.*, 2022, **12**, 2201713.

11 Y. Jiao, Y. Zheng, M. Jaroniec and S. Z. Qiao, Design of electrocatalysts for oxygen- and hydrogen-involving energy conversion reactions, *Chem. Soc. Rev.*, 2015, **44**, 2060–2086.

12 W. Xu, Z. Lu, X. Sun, L. Jiang and X. Duan, Superwetting electrodes for gas-involving electrocatalysis, *Acc. Chem. Res.*, 2018, **51**, 1590–1598.

13 M. F. Lagadec and A. Grimaud, Water electrolysers with closed and open electrochemical systems, *Nat. Mater.*, 2020, **19**, 1140–1150.

14 C. Qi, F. Jiang and S. Yang, Advanced honeycomb designs for improving mechanical properties: A review, *Composites, Part B*, 2021, **227**, 109393.

15 J. Zhang, G. Lu and Z. You, Large deformation and energy absorption of additively manufactured auxetic materials and structures: A review, *Composites, Part B*, 2020, **201**, 108340.

16 C. C. McCrory, S. Jung, J. C. Peters and T. F. Jaramillo, Benchmarking heterogeneous electrocatalysts for the oxygen evolution reaction, *J. Am. Chem. Soc.*, 2013, **135**, 16977–16987.

17 W. Zheng, M. Liu and L. Y. S. Lee, Best practices in using foam-type electrodes for electrocatalytic performance benchmark, *ACS Energy Lett.*, 2020, **5**, 3260–3264.

18 X. Li, J. Zhou, C. Liu, L. Xu, C. Lu, J. Yang, H. Pang and W. Hou, Encapsulation of janus-structured Ni/Ni_2P nanoparticles within hierarchical wrinkled n-doped carbon nanofibers: Interface engineering induces high-efficiency water oxidation, *Appl. Catal., B*, 2021, **298**, 120578.

19 W. Cheng, S. Xi, Z.-P. Wu, D. Luan and X. W. Lou, *In situ* activation of Br-confined Ni-based metal-organic framework hollow prisms toward efficient electrochemical oxygen evolution, *Sci. Adv.*, 2021, **7**, eabk0919.

20 H. Zhang, W. Zhou, J. Dong, X. F. Lu and X. W. Lou, Intramolecular electronic coupling in porous iron cobalt (oxy)phosphide nanoboxes enhances the electrocatalytic activity for oxygen evolution, *Energy Environ. Sci.*, 2019, **12**, 3348–3355.

21 J. Duan, S. Chen and C. Zhao, Ultrathin metal-organic framework array for efficient electrocatalytic water splitting, *Nat. Commun.*, 2017, **8**, 15341.

22 K. Yue, J. Liu, C. Xia, K. Zhan, P. Wang, X. Wang, Y. Yan and B. Y. Xia, Controllable synthesis of multidimensional carboxylic acid-based NiFe MOFs as efficient electrocatalysts for oxygen evolution, *Mater. Chem. Front.*, 2021, **5**, 7191–7198.

23 Y. Sun, S. Xu, C. A. Ortiz-Ledon, J. Zhu, S. Chen and J. Duan, Biomimetic assembly to superplastic metal-organic framework aerogels for hydrogen evolution from seawater electrolysis, *Exploration*, 2021, **1**, 20210021.

24 L. F. Marques, H. P. Santos, C. C. Correa, J. A. L. C. Resende, R. R. da Silva, S. J. L. Ribeiro and F. C. Machado, Construction of a series of rare earth metal-organic frameworks supported by thiophenedicarboxylate linker: Synthesis, characterization, crystal structures and near-infrared/visible luminescence, *Inorg. Chim. Acta*, 2016, **451**, 41–51.

25 G. X. Wang, L. L. Shang, Z. H. Li and B. T. Zhao, A new two-dimensional manganese(II) coordination polymer based on thiophene-3,4-dicarboxylic acid, *Acta Crystallogr., Sect. C: Struct. Chem.*, 2014, **C70**, 715–717.

26 H. Fei, X. Liu, Z. Li and W. Feng, Synthesis of manganese coordination polymer microspheres for lithium-ion batteries with good cycling performance, *Electrochim. Acta*, 2015, **174**, 1088–1095.

27 X. Chen, L. Zhang, W. Xu, X. Ding, S. Chen, X. She, X. Guo, C.-L. Dong, Y. Huang, L. Zhang, S. Shen and D. Yang, Biochar aerogel decorated with thiophene S manipulated 5-membered rings boosts nitrogen fixation, *Appl. Catal., B*, 2022, **313**, 121425.

28 F. Sun, G. Wang, Y. Ding, C. Wang, B. Yuan and Y. Lin, NiFe-based metal-organic framework nanosheets directly supported on nickel foam acting as robust electrodes for electrochemical oxygen evolution reaction, *Adv. Energy Mater.*, 2018, **8**, 1800584.

29 S. Hu, Y. Li, D. Kim, M. Liu, L. Y. S. Lee and K. Y. Wong, Surface modulated Fe doping of β-$Ni(OH)_2$ nanosheets for highly promoted oxygen evolution electrocatalysis, *EcoMat*, 2022, **4**, e12256.

30 Z. Wan, D. Yang, J. Chen, J. Tian, T. T. Isimjan and X. Yang, Oxygen-evolution catalysts based on iron-mediated nickel metal–organic frameworks, *ACS Appl. Nano Mater.*, 2019, **2**, 6334–6342.

31 Q. Hu, Z. Wang, X. Huang, Y. Qin, H. Yang, X. Ren, Q. Zhang, J. Liu, M. Shao and C. He, Integrating well-controlled core-shell structures into ''superaerophobic'' electrodes for water oxidation at large current densities, *Appl. Catal., B*, 2021, **286**, 119920.

32 Y. Bai, Y. Wu, X. Zhou, Y. Ye, K. Nie, J. Wang, M. Xie, Z. Zhang, Z. Liu, T. Cheng and C. Gao, Promoting nickel oxidation state transitions in single-layer NiFeB hydroxide nanosheets for efficient oxygen evolution, *Nat. Commun.*, 2022, **13**, 6094.

33 Z. Gong, R. Liu, H. Gong, G. Ye, J. Liu, J. Dong, J. Liao, M. Yan, J. Liu, K. Huang, L. Xing, J. Liang, Y. He and H. Fei, Constructing a graphene-encapsulated amorphous/crystalline heterophase NiFe alloy by microwave thermal shock for boosting the oxygen evolution reaction, *ACS Catal.*, 2021, **11**, 12284–12292.

34 S. Zou, M. S. Burke, M. G. Kast, J. Fan, N. Danilovic and S. W. Boettcher, Fe(oxy)hydroxide oxygen evolution reaction electrocatalysis: Intrinsic activity and the roles of electrical conductivity, substrate, and dissolution, *Chem. Mater.*, 2015, **27**, 8011–8020.

35 S. Anantharaj, S. Kundu and S. Noda, ''The Fe effect'': A review unveiling the critical roles of Fe in enhancing oer activity of Ni andCo based catalysts, *Nano Energy*, 2021, **80**, 105514.

36 H. Xiao, H. Shin and W. A. Goddard, Synergy between Fe and Ni in the optimal performance of (Ni,Fe)OOH catalysts for the oxygen evolution reaction, *Proc. Natl. Acad. Sci. U. S. A.*, 2018, **115**, 5872–5877.

37 C. F. Li, L. J. Xie, J. W. Zhao, L. F. Gu, H. B. Tang, L. Zheng and G. R. Li, Interfacial Fe–O–Ni–O–Fe bonding regulates the active Ni sites of Ni-MOFs via iron doping and decorating with FeOOH for super-efficient oxygen evolution, *Angew. Chem., Int. Ed.*, 2022, **61**, e202116934.

38 Y. Zhao, X. F. Lu, Z. P. Wu, Z. Pei, D. Luan and X. W. D. Lou, Supporting trimetallic metal-organic frameworks on S/N-doped carbon macroporous fibers for highly efficient electrocatalytic oxygen evolution, *Adv. Mater.*, 2023, **35**, 2207888.

39 M. Fang, X. Gao, J. Liang, B. Guo, L. Zou, J. Lu, Y. Gao, E. C. M. Tse and J. Liu, Bioinspired NiFe-gallate metal-organic frameworks for highly efficient oxygen evolution electrocatalysis, *J. Mater. Chem. A*, 2022, **10**, 7013–7019.

40 L. Trotochaud, S. L. Young, J. K. Ranney and S. W. Boettcher, Nickel-iron oxyhydroxide oxygen-evolution electrocatalysts: The role of intentional and incidental iron incorporation, *J. Am. Chem. Soc.*, 2014, **136**, 6744–6753.

41 D. Friebel, M. W. Louie, M. Bajdich, K. E. Sanwald, Y. Cai, A. M. Wise, M. J. Cheng, D. Sokaras, T. C. Weng, R. Alonso-Mori, R. C. Davis, J. R. Bargar, J. K. Norskov, A. Nilsson and A. T. Bell, Identification of highly active Fe sites in (Ni,Fe)OOH for electrocatalytic water splitting, *J. Am. Chem. Soc.*, 2015, **137**, 1305–1313.

42 J. Wang, N. Zang, C. Xuan, B. Jia, W. Jin and T. Ma, Self-supporting electrodes for gas-involved key energy reactions, *Adv. Funct. Mater.*, 2021, **31**, 2104620.

43 B. Wang, M. Zhao, L. Li, Y. Huang, X. Zhang, C. Guo, Z. Zhang, H. Cheng, W. Liu, J. Shang, J. Jin, X. Sun, J. Liu and H. Zhang, Ultra-thin metal-organic framework nanoribbons, *Natl. Sci. Rev.*, 2020, **7**, 46–52.

44 M. B. Stevens, L. J. Enman, A. S. Batchellor, M. R. Cosby, A. E. Vise, C. D. M. Trang and S. W. Boettcher, Measurement techniques for the study of thin film heterogeneous water oxidation electrocatalysts, *Chem. Mater.*, 2016, **29**, 120–140.

45 H. S. Ahn and A. J. Bard, Surface interrogation scanning electrochemical microscopy of $Ni_{1-x}Fe_xOOH$ $(0 < x < 0.27)$ oxygen evolving catalyst: Kinetics of the ''fast'' iron sites, *J. Am. Chem. Soc.*, 2016, **138**, 313–318.

46 M. Lu, Y. Zheng, Y. Hu, B. Huang, D. Ji, M. Sun, J. Li, Y. Peng, R. Si, P. Xi and C.-H. Yan, Artificially steering electrocatalytic oxygen evolution reaction mechanism by regulating oxygen defect contents in perovskites, *Sci. Adv.*, 2022, **8**, eabq3563.

47 F. Cheng, Z. Li, L. Wang, B. Yang, J. Lu, L. Lei, T. Ma and Y. Hou, In situ identification of the electrocatalytic water oxidation behavior of a nickel-based metal-organic framework nanoarray, *Mater. Horiz.*, 2021, **8**, 556–564.

48 J. Y. Chen, L. Dang, H. Liang, W. Bi, J. B. Gerken, S. Jin, E. E. Alp and S. S. Stahl, Operando analysis of NiFe and Fe oxyhydroxide electrocatalysts for water oxidation: Detection of Fe^{4+} by mossbauer spectroscopy, *J. Am. Chem. Soc.*, 2015, **137**, 15090–15093.

49 L. J. Enman, M. S. Burke, A. S. Batchellor and S. W. Boettcher, Effects of intentionally incorporated metal cations on the oxygen evolution electrocatalytic activity of nickel (oxy)hydroxide in alkaline media, *ACS Catal.*, 2016, **6**, 2416–2423.

50 L. Yu, S. Sun, H. Li and Z. J. Xu, Effects of catalyst mass loading on electrocatalytic activity: An example of oxygen evolution reaction, *Fundam. Res.*, 2021, **1**, 448–452.

